ADVANCED FUNCTIONAL MATERIALS
www.afm-journal.de

Decoding the Broadband Emission of 2D Pb-Sn Halide Perovskites through High-Throughput Exploration

Elham Foadian, Jonghee Yang, Sumner B. Harris, Yipeng Tang, Christopher M. Rouleau, Syed Joy, Kenneth R. Graham, Benjamin J. Lawrie, Bin Hu, and Mahshid Ahmadi**

Unlike single-component 2D metal halide perovskites (MHPs) exhibiting sharp excitonic photoluminescence (PL), a broadband PL emerges in mixed Pb-Sn 2D lattices. Two physical models –self-trapped exciton and defect-induced Stokes-shift – are proposed to explain this unconventional phenomenon. However, the explanations provide limited rationalizations without consideration of the formidable compositional space, and thus, the fundamental origin of broadband PL remains elusive. Herein, the high-throughput automated experimental workflow is established to systematically explore the broadband PL in mixed Pb-Sn 2D MHPs, employing PEA (Phenethylammonium) as a model cation known to work as a rigid organic spacer. Spectrally, the broadband PL becomes further broadened with rapid PEA_2PbI_4 phase segregation with increasing Pb concentrations during early-stage crystallization. Counterintuitively, MHPs with high Pb concentrations exhibit prolonged PL lifetimes. Hyperspectral microscopy identifies substantial PEA_2PbI_4 phase segregation in those films, hypothesizing that the establishment of charge transfer excitons by the phase segregation upon crystallization at high-Pb compositions results in distinctive PL properties. These results indicate that two independent mechanisms—defect-induced Stoke-shifts and the establishment of charge transfer excitons by phase segregation—coexist which significantly correlates with the Pb:Sn ratio, thereby simultaneously contributing to the broadband PL emission in 2D mixed Pb-Sn HPs.

1. Introduction

The exceptional optical and electronic characteristics and affordability of metal halide perovskites (MHPs) have generated significant interest in the field of optoelectronic materials.[1] In recent years, 2D MHPs have gained notable attention for their immense promise in various optoelectronic applications, including solar cells and light-emitting diodes.[2,3] Moreover, compared to 3D organic–inorganic halide perovskites, 2D MHPs offer a compelling advantage due to their unique quantum well structure which results in the efficient confinement of charge carriers within the inorganic layer and enhances their stability.[4] Higher stability is a key factor that makes 2D structures a promising choice in various applications, ensuring better long-term performance and reliability.[5]

A significant obstacle in advancing perovskite devices for widespread commercial use is the negative environmental impact due to the presence of toxic Pb.[6] Among various elements considered as replacements for Pb^{2+}, Sn^{2+} stands out as the most promising candidate which shares similar ionic radius (112 and 120 pm for Sn^{2+} and Pb^{2+}, respectively[7,8]) and electronic structures.[9] Additionally, due to their closely matched elemental properties, Pb and Sn can be seamlessly integrated into a solid solution, forming a mixed Sn–Pb compound in any desired proportion.[10] Considering these compatibilities, substitution of Pb with Sn in MHPs could be a significant step forward in addressing health and environmental concerns associated with Pb-based alternatives,[11] and has led to extensive research aimed at developing environmentally friendly and sustainable MHP platforms.[12]

Interestingly, mixed Pb-Sn 2D perovskites differ from their 3D counterparts as their spectra are dominated by sub-bandgap

E. Foadian, J. Yang, Y. Tang, B. Hu, M. Ahmadi
Institute for Advanced Materials and Manufacturing
Department of Materials Science and Engineering
University of Tennessee
Knoxville, TN 37996, USA
E-mail: jhyang@yonsei.ac.kr; mahmadi3@utk.edu
J. Yang
Department of Chemistry
Yonsei University
Seoul 03722, Republic of Korea
The ORCID identification number(s) for the author(s) of this article can be found under https://doi.org/10.1002/adfm.202411164
S. B. Harris, C. M. Rouleau, B. J. Lawrie
Center for Nanophase Materials Sciences
Oak Ridge National Laboratory
Oak Ridge, TN 37831, USA
S. Joy, K. R. Graham
Department of Chemistry
University of Kentucky
Lexington, KY 40506, USA
B. J. Lawrie
Materials Science and Technology Division
Oak Ridge National Laboratory
Oak Ridge, TN 37831, USA

DOI: 10.1002/adfm.202411164

broadband emissions rather than band-edge emissions, which still the origin of them remains a topic of debate and uncertainty.[9b] The broad emission in mixed Pb-Sn 2D MHPs could potentially be attributed to self-trapped excitons (STEs)[13] or structural defects of the material, the latter hypothesizing that excitons become confined within the defect-induced sub-bandgap trap states and undergo radiative relaxation by Stokes shifts.[13a,14] In this context, Li et al. claimed that Sn-doped PEA_2PbI_4 (PEA = Phenethylammonium) have a strong broadband emission which is attributed to Sn-triggered extrinsic STE.[14a] On the other hand, Fang et al. found that the insensitivity of broadband emission to the Pb-Sn ratio and slower decay suggested defects, not exciton self-trapping, as the source of this emission in 2D Pb-Sn perovskite alloys.[15] Meanwhile, Zhang et al. claimed that the broadband emission observed in PEA_2PbI_4/PEA_2SnI_4 double-layer heterostructures may be caused by charge transfer (CTE) emission at the PEA_2PbI_4:PEA_2SnI_4 interfaces.[16]

So far, the broadband emission in 2D mixed Pb-Sn MHP systems has been mainly explored based on the physics perspective with the limited MHP compositions, relying on the understanding of exciton dynamics and lattice behaviors in such representative conditions. However, this approach conversely deters the understanding of the global spectral feature emerging in this compositional space. Furthermore, the lattice features and the resulting excitonic behaviors can also vary depending on the synthetic parameters, particularly responsible for the defects formation in this materials system.[17] Thus, the details in the broadband spectral evolution, where its control is important for some applications including white-light generation,[18] as well as its genuine origin in 2D mixed Pb-Sn MHP system has not been comprehensively understood so far. Recently, high-throughput robotics synthesis platforms have introduced a fresh opportunity for investigating and enhancing materials processing techniques.[19,20] The lack of advanced tools restricted progress in finding useful material combinations, therefore, it's crucial to emphasize the need for creating a high-throughput experimental approach to investigate various Pb-Sn combinations in 2D perovskite materials to understand the origin of their broadband emission, which hasn't been done yet.

Herein, we comprehensively explore the intriguing fundamental spectral behaviors in mixed Pb-Sn 2D MHPs by utilizing a high-throughput automated synthesis-characterization workflow. 2D MHP microcrystals with 96 different Pb-Sn ratios are synthesized in a microplate through combinatorial mixing of PEA_2PbI_4 and PEA_2SnI_4 precursors solution and subsequent crystallization. High-throughput optical characterization allows for efficient exploration of the serial changes of PL spectral features including the broadband emission as a function of Pb-Sn ratios over time, which cannot be expedited by human efforts.

We observe that the broadband emission globally emerges in every mixed-compositional range, and the spectral feature becomes further broadened with increasing Pb concentration. Also, phase separation of PEA_2PbI_4 from the mixed Pb-Sn 2D MHPs takes place over time in photoluminescence results, which is facilitated with increasing Pb concentration. X-ray based chemical and structural analysis revealed that, counterintuitively, the amounts of defects (i.e., iodine vacancies) species are exponentially proportional to the Pb concentrations in the 2D MHPs, which is irrespective of the ambient exposure particularly in Pb-rich cases. This indicates that, for Pb-rich compositions, those defects are inherently formed upon synthesis and not fully incorporated well into the inorganic lattice. Hyperspectral cathodoluminescence (CL) microscopy reveals the segregated PEA_2PbI_4 phase in those films as seen in early-stage crystallization behaviors evidenced by high-throughput observations. We hypothesize that the inherent, uncontrolled segregation of the PEA_2PbI_4 phase upon crystallization at high-Pb compositions establish charge transfer states dominant in the 2D MHP matrix, far outperforming the defect-induced emission – valid for the system with nominal Pb concentrations – and thereby resulting in PL broadening and longer lifetimes. Our high-throughput approach successfully resolves the prior controversies surrounding the origin of broadband emissions in 2D mixed Pb-Sn MHPs, offering a comprehensive understanding of the fundamental principles and practical applications of these intricate material systems.

2. Results and Discussion

2.1. High-Throughput Exploration of Broadband Emission in Mixed Pb-Sn 2D MHPs

Essentially, the photophysics of materials is largely dependent on a multitude of factors having profound correlations with the crystallite lattice. Two distinctive factors, defects and phase separations, are known to substantially tune the emission features. While extensive efforts have been made to control these obstacles in 3D MHPs, similar investigations for mixed Pb-Sn 2D MHPs, which possess nontrivial chemical complexity, have not been seriously considered.[21] Given these materials are synthesized via simple solution processing, a comprehensive understanding of the crystallization dynamics is primarily necessary for the exploration of the complex fundamental properties. Recently, we have successfully demonstrated that our high-throughput automated synthesis-characterization workflow provides a systematic understanding of the early-stage crystallization dynamics of low-dimensional MHPs, allowing us to gain fundamental insights into the functional materials systems.[19a]

Encouraged by this, to effectively explore the evolution of the broadband PL in a Pb-Sn compositional space of the 2D MHPs, we implement a high-throughput automated experimental workflow, as shown in **Figure 1**. By utilizing an automated pipetting robot, we systematically mix PEA_2PbI_4 and PEA_2SnI_4 precursor solutions with 96 different ratios in a microplate and subsequently synthesize the mixed Pb-Sn 2D MHP crystallites via antisolvent (e.g., toluene) injection within an hour (Figure 1a; Figure S1, Supporting Information).[19a,c,d] After mixing, the microplate is sealed and quickly transferred to an optical reader to characterize the PL properties of each binary composition of 2D MHP over time (for 1000 min). Monitoring the PL changes over time provides insights into the early-stage crystallization behaviors – difficult to explore in the conventional film fabrication process – of 2D MHPs in the Pb-Sn compositional space (Figure 1b). The time evolution of PL spectra determines the defect densities and chemical inhomogeneities in the solution-processed materials associated with the broadband emission.[19a]

Practically, the time-evolved PL characterization produces 9600 individual PL spectra in a dataset (96 wells in a plate

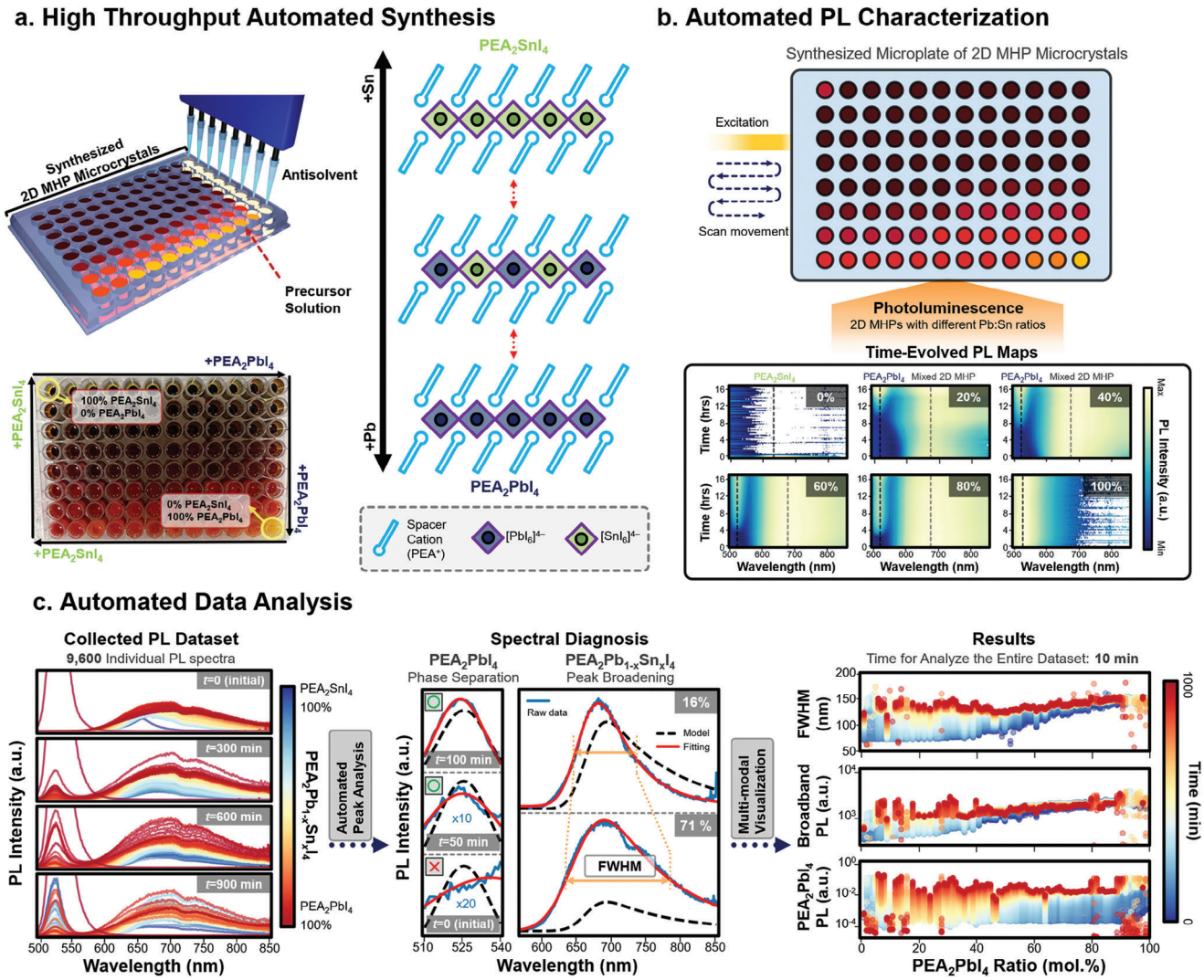

Figure 1. Experimental workflow showing the automated high-throughput exploration of 2D Pb-Sn MHPs. a) High-throughput automated synthesis of the 2D MHP microcrystals via combinatorial mixing of PEA_2PbI_4 and PEA_2SnI_4 endmember precursors using the pipetting robot and subsequent antisolvent (toluene) injection, allowing the synthesis of 96 different binary mixtures. b) High-throughput automated time-evolved PL characterizations using an optical reader, providing 9600 individual PL spectra for 1000 min. c) Spectral diagnosis of PL dataset via implementation of automated peak fitting function, allowing for comprehensive monitoring of PL characteristics for each composition over time. Analyzing the entire dataset takes only 10 min.

multiplied by 100 measurement cycles; Figure S2, Supporting Information), which is impractical to be analyzed solely by human efforts. To address this challenge, a Python-based automated peak-fitting and tracking function is designed and implemented (Figure 1c).[19a] Here, we implement symmetric (Gaussian) and asymmetric (exponentially modified Gaussian) peak models for segregated PEA_2PbI_4 (vide infra) and broadband emissions, respectively. This peak-fitting function significantly streamlines the analysis of high-throughput observations, which automatically and accurately measures the PL properties including full-width at half-maximum (FWHM) and intensity for each peak component in the entire dataset within only 10 min. As a result, the overall workflow allows for a comprehensive and accelerated understanding of the crystallization dynamics in 2D MHPs across the Pb-Sn compositional space.

Figure 2a shows the PL spectral maps of the 2D MHP microcrystals across the Pb-Sn compositional space at three different timepoints: initial, 5, and 10 h, respectively, showing a global trend in the evolution of emission behaviors over time (corresponding overlays of PL spectra are shown in Figure S3a, Supporting Information). Except for pure PEA_2SnI_4 and PEA_2PbI_4 showing respective band-edge excitonic emission peaks at ≈620 and ≈525 nm, respectively (Figure S4, Supporting Information),[13a,16,22] initially, all mixed Pb-Sn 2D MHP microcrystals exhibit a broadband emission peaked at ≈700 nm involving a shoulder at 750 nm, which corresponds to the photoluminescence peak of 2D Pb-Sn perovskites.[23] It is evident that an increase in the PEA_2PbI_4 ratio initially broadens the broadband emission, and as time progresses, the broad emission continues to widen – particularly at the low-Pb compositions

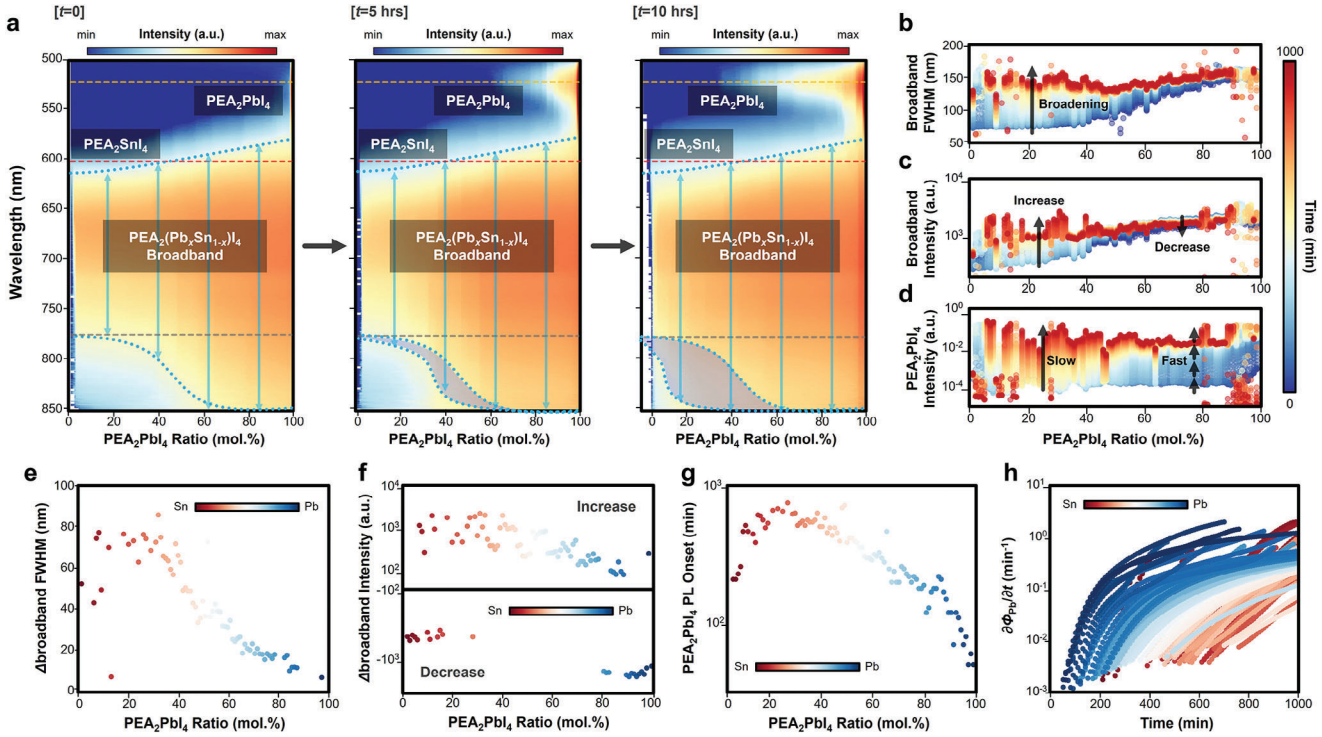

Figure 2. a) 2D spectro-compositional maps of the mixed Pb-Sn 2D MHP microcrystals photoluminescence at three different time-points across the compositional space, which were synthesized by high-throughput automated synthesis. Temporal changes in b) broadband FWHM, c) broadband PL intensity, and d) PEA_2PbI_4 PL intensity in the mixed Pb-Sn 2D MHP microcrystals across the Pb-Sn compositional space. Difference of e) FWHM (ΔFWHM) and f) broadband intensity (Δbroadband intensity) between the initial and final time-points as a function of Pb compositional ratio. g) The onset timepoints of PEA_2PbI_4 peak, and h) 1st derivative of PEA_2PbI_4 PL intensity (corresponding to transient growth rates of PEA_2PbI_4 phase) as a function of Pb compositional ratio.

(color-marked areas in the maps). Such dynamic changes suggest that there is an indirect relationship between the broadband features and Pb-Sn compositions; rather than the composition itself. Therefore, there are likely secondary factors associated with the peak broadening, the behaviors of which strongly depend on the Pb-Sn composition. Given the distinctive difference in PL intensity and stability between both endmembers (i.e., PEA_2SnI_4 and PEA_2PbI_4) respectively reflecting the defect formation rates and crystal growth (Figure S4, Supporting Information),[24] the emergence of defects as consequences of incompatible chemical stability and crystallization rate can be responsible for the broadband feature in the mixed Pb-Sn MHP system. Indeed, defects in the lattice, particularly the iodine vacancies at apical direction, have been suggested to be the origin of the broadband emission,[9b,25] which could be produced upon crystallization.

Interestingly, an additional PEA_2PbI_4 PL is observed in the MHP microcrystals across the Pb-Sn compositional space over time, which initially emerges at high-Pb compositions and gradually expands to lower Pb compositions over time (Figure S3b, Supporting Information). This indicates that phase segregation of metal cations occurs during crystallization, and the rate of crystallization depends on the Pb-Sn compositions. To gain a more detailed understanding of the PL behaviors in this materials system, we explore the time-evolved PL spectra of mixed Pb-Sn MHP microcrystals with selected compositional ratios, as visualized in Figure S5 (Supporting Information). Overall, two global features are observed: with increasing Pb composition ratios, a) the initial broadband becomes wider, and b) the emergence of PEA_2PbI_4 peaks becomes faster (from 600 to <100 min after antisolvent injection). We note that, specifically, the 2D MHP microcrystals with low Pb ratios (i.e., 10 to 40%) exhibit a sudden widening of the broadband at respective timepoints, which qualitatively coincides with the time onset of the PEA_2PbI_4 PL emergence. This suggests a strong correlation between the broadband emission and the segregated PEA_2PbI_4 phase, which is plausible as the charge transfer state can be established between the segregated lattice and the mixed Pb-Sn 2D MHPs.[16]

To ensure the formation of 2D perovskite phases in the solution, UV–vis absorption and PL characterization are performed on the microcrystals before the injection of any antisolvent (Figure S6, Supporting Information). The emission spectra differ significantly from those obtained after antisolvent injections without any PL or absorption peaks, clearly demonstrating that the high-throughput PL spectra reflect the emission behaviors of 2D MHPs phases. In addition, the X-ray Diffraction patterns (XRD) of the microcrystals, representing three selected Pb:Sn compositions (Figure S7, Supporting Information), exhibit distinctive diffraction patterns characteristic of 2D MHPs confirming the formation of 2D MHPs microcrystals in the solution.[16]

Through comprehensive analysis of PL dataset by the implementation of the peak-fitting function, the detailed parameters (i.e., broadband FWHM, evolutions of broadband, and

segregated PEA_2PbI_4 peak intensities) in time-evolved PL emissions are quantified across the Pb-Sn compositional space, as visualized in Figure 2b–d. Initially, the FWHM of broad emission expands from 60 to 170 nm with increasing Pb composition ratios from 1% to 99%. Such a significant difference in FWHM suggests that different mechanisms are associated with the emission behaviors of 2D mixed Pb-Sn MHPs at the low- and high-Pb compositional ranges. Also, the broadband continues to widen over 1000 min as shown in Figure 2b. Figure 2e shows the difference in FWHM (ΔFWHM) between the initial and final time (after 1000 min) as a function of Pb-Sn compositions, showing more pronounced peak broadening of ≈80 nm in the MHPs with low-Pb compositional ratios over time. As a result, the broadband FWHMs exhibit nominal values >120 nm across the entire compositional space, suggesting that the broadband emission mechanism at low-Pb 2D MHPs likely transforms to that of high-Pb counterparts.

Figure 2c shows the temporal evolution of broadband emission intensity across the Pb-Sn compositional space. Except for the MHPs with <20% Pb showing PL drops – as a result of rapid degradation by Sn oxidation (Figure S4, Supporting Information),[22,26] for the MHPs with low-Pb compositions, intensity consistently increases (Figure 2f). Given the favorable oxidation and the consequent degradation of 2D Sn and low-Pb MHPs under ambient conditions, which promote defect formations over time, the temporal enhancements of broadband PL in low-Pb 2D MHPs seemingly support the scenario of defect-induced Stokes-shift contributing to broadband emission; The widening of the broadband in this compositional range also seems to align with this scenario. In contrast, for the MHPs with high-Pb compositions, an initial enhancement in broadband PL intensity is followed by a reduction. While such an up-and-down trend can be attributed to the competition between the slower crystallite growths and slower degradation – Pb^{2+} is more stable than Sn^{2+} upon ambient oxidation – the trend is irrespective of the continuous (though slow) widening of the broadband. In fact, not only defects associated with broadband emission, the degradation of MHP crystallites also produces defects promoting non-radiative recombination compromising PL intensity.[15a] These observations strongly suggest that defects and phase segregation of PEA_2PbI_4 concurrently contribute to peak broadening. In addition, given the similarity in diffusion coefficients between Sn^{2+} and Pb^{2+},[27] along with lattice reorganization being dependent on defective sites, it can be hypothesized that the formation of PEA_2PbI_4 is more attributable to phase segregation than any lattice reorganization. Furthermore, the oxidation of Sn is unlikely to contribute to the formation of this component, as compositions with higher Pb content exhibit more PEA_2PbI_4. This suggests that the presence and ratio of Pb play a more critical role in the formation process, discounting Sn oxidation as a primary factor.

Now we focus on the segregation behavior of PEA_2PbI_4 peak across the compositional space. As shown in Figure 2d, notably faster PEA_2PbI_4 PL emergences are observed with increasing Pb composition ratios. From the intensity profiles, the onset timepoints of PEA_2PbI_4 peak are estimated across the compositional space (Figure 2g). Evidently, for the low-Pb compositions, the emergences of PEA_2PbI_4 peak are first observed over several 100 min after antisolvent addition, whereas those of the MHPs with high-Pb compositions are detected within 100 min. These observations indicate that the segregation of PEA_2PbI_4 from the mixed Pb-Sn MHP phase becomes substantially accelerated with increasing Pb composition ratios. Note that the emergences of PEA_2SnI_4 are difficult to be identified and deconvoluted from the PL spectra, mainly due to the weak PLQY and the spectral proximity of the peak with the broadband.[28] In addition, considering the ambient-susceptible nature of Sn^{2+} leading to temporal degradation with substantial PL quenching via defect-induced non-radiative recombination, the contribution of PEA_2SnI_4 in the spectral feature of the 2D mixed Pb-Sn MHPs would be negligible. It is also noteworthy that the MHP microcrystals with <20% Pb compositions exhibit relatively faster PEA_2PbI_4 peak emergences compared with the nominal level of MHPs with intermediate Pb compositions. This can be explained by the rapid oxidation of Sn^{2+} in the inorganic lattice, which accelerates the uncontrollable phase changes upon degradation. In addition, it is noteworthy that if phase segregation was to compromise the 2D structure, this would typically result in the degradation of the broad emission spectrum. However, it has been observed that compositions with higher Pb content, despite experiencing greater phase segregation, still exhibit an expanded broad emission spectrum over time.

To understand the kinetic aspects in PEA_2PbI_4 segregation, we take the first derivatives of PEA_2PbI_4 PL intensities with respect to the reaction time (i.e., $\partial\Phi_{Pb}/\partial t$) for the entire compositional space, as shown in Figure 2h. Notably faster growth rates of PEA_2PbI_4 (1–2 orders of magnitudes) are observed at the earlier timepoints (<200 min) for high-Pb 2D MHPs compared with the low-Pb counterparts. This indicates that the substantial phase segregation takes place at a very early-time during crystallization at high-Pb compositions. In contrast, at the intermediate-Pb compositions, the rate of PEA_2PbI_4 segregation starts to slowly increase later after 200–600 min. Note that very small PL intensity of the segregated PEA_2PbI_4 crystallites below the detection limit of the instrument, attributed to their extremely small amounts, may not be collected during the measurement. However, the observed trends qualitatively suggest that phase separation takes place at the very initial time with extremely low intensity (Figure S3b, Supporting Information), as evidenced by the large FWHM of the broadband even at the initial PL spectra for Pb-rich MHP microcrystallites.

Overall, these results indicate that the segregation behavior of PEA_2PbI_4 phase in 2D mixed Pb-Sn MHPs becomes substantial with increasing Pb compositions. Inevitably, this can result in the non-trivial emergence of the segregated PEA_2PbI_4 phase during the crystallization of Sn-doped PEA_2PbI_4 thin films (vide infra) that have been prepared for photophysical investigations,[9b,15a,25] which, surprisingly, has been somewhat overlooked from interpretation so far.

Note that the temporal evolutions for the PL parameters across the Pb-Sn compositional space share consistent trends with each other; gradually, the parameters undergo notable changes for the MHP microcrystals with low-Pb compositions, whereas those at high-Pb compositions show mild changes (or quickly reach the saturation level in PEA_2PbI_4 intensity) over time. Although defects contribute more significantly to peak broadening in compositions with lower Pb content, as the Pb content increases and time progresses, the segregated phase of

PEA_2PbI_4 becomes more prominent; this enhanced segregation has an increasingly greater impact on the broadening of the PL peaks.

2.2. Experimental Characterization of Mixed Pb-Sn 2D MHPs Thin Films

After high-throughput exploration of the crystallization behaviors in mixed Pb-Sn 2D MHPs, now we investigate the PL characteristics of the MHP thin films to understand how the early-stage crystallization behaviors influence the chemical inhomogeneity and optical properties of the resulting films. Here, in addition to PEA_2SnI_4 and PEA_2PbI_4 endmembers, we select five mixed Pb-Sn compositions with a serial increase of Pb compositional ratio (i.e., 10, 35, 60, 85, and 96%) and the corresponding 2D MHP films were prepared via spin coating method. PL spectra were measured for two different solvents and annealing temperatures, identifying the optimal conditions of film fabrication (Experimental Section, Figures S8 and S9, Supporting Information). Figure S10a (Supporting Information) shows UV–vis absorption spectra of the films, revealing serial blueshifts of the excitonic peak with increasing Pb compositional ratios. Note that the films with high-Pb ratios (i.e., 85 and 96%) exhibit distinctive excitonic peaks of PEA_2PbI_4 separated from the corresponding absorption edge, which is not observed in Sn-rich films. This infers notable segregation action of PEA_2PbI_4 phase in the films at high-Pb ratios. Moreover, the shoulder peak observed at 380 nm is likely associated with the intrinsic energy state of PEA_2PbI_4.[29] Similarly, the more diffused peak at 525 nm, observed at a Pb = 0 concentration, correlates with the intrinsic energy state of PEA_2SnI_4.[30] From the corresponding Tauc plots, the optical bandgap (E_g) of the mixed phases is estimated and it reveals that the E_g of the films exhibits an exponential increase from 1.94 to 2.35 eV with increasing Pb ratios (Figure S10b,c, Supporting Information). The non-linear trend in E_g profile deviating from Vegard's law could be attributed to the energy mismatch of the Pb 6s and Sn 5s states in the valence band.[31] Additionally, significant phase segregation such as with the 85 and 96% samples can complicate the extraction of the bandgap and can explain the perceived deviation from Vegard's law since the absorbance would be a linear combination of the separate phases. We also estimated Urbach tail energy (E_u) in the film matrices,[32] as shown in Figure S10d (Supporting Information). Except for PEA_2PbI_4, a gradual increase in E_u from 280 to 380 meV is observed with increasing Pb ratios, indicating the qualitative increase of Pb results in higher energetic disorder at the band-tail states in the mixed Pb-Sn 2D MHPs.[33] This could be attributed to the phase segregation and/or the defect densities formed in the films.

Figure S11a (Supporting Information) shows time-evolved PL spectra of mixed Pb-Sn 2D MHP thin films. Similar to the high-throughput observations, here the broadband emission becomes wider with increasing Pb composition ratios. Particularly, tiny but evident bumps of PEA2PbI4 emission at ≈522 nm are also observed for the films with Pb composition ratios over 60%, which indeed confirms that phase segregation occurs upon the film crystallization at high Pb ratios. The emergence of PEA2PbI4 is not appreciable in the film with 10 and 35% Pb ratios, suggesting that the retarded and slow segregation behaviors observed in the solution phase are reflected as the suppression of the segregation at these ranges.

We implement the devised peak-fitting function to analyze the time-evolution of PL features in the films, as shown in Figure S11b–d (Supporting Information). In Figure S11b (Supporting Information) it is shown that the temporal changes in broadband FWHM for low-Pb films are negligible, far different from the dynamic changes observed in the microcrystal system. Moreover, the FWHM values of the low-Pb 2D MHPs exhibit nominal values of ≈80 nm, whereas those of high-Pb MHPs show distinctively large values of 120–180 nm. This indicates that the physicochemical action associated with the widening of the broadband – hypothesized to be PEA_2PbI_4 segregation that establishes charge transfer exciton (CTE) states – shown in microcrystal analysis is suppressed in the low-Pb films. The retarded and slow PEA_2PbI_4 segregation shown in high-throughput results of low-Pb MHPs support this, as the ion movement is deemed to be restricted in the solid matrix compared to the situation corresponds to the microcrystals system in the solution phase.[19a] The stronger bond dissociation energy of Sn-I (234 kJ mol^{-1}) compared to that of Pb-I (197 kJ mol^{-1}) also supports this. Meanwhile, the temporal drops of broadband PL intensity in all films, as a result of ambient degradation can be observed (Figure S11c, Supporting Information).[34] Collectively with the constant FWHM despite the increase in defects by temporal degradation, these observations indicate that these defects are unlikely to be the only cause of changes in the broadband features.

The PL intensity of the segregated PEA_2PbI_4 phase in the films over time directly corroborates the negligible phase segregation in the low-Pb films, which is, in contrast, distinctive in the films with high Pb compositions with stronger PL (Figure S11d, Supporting Information). Note that the PEA_2PbI_4 intensity profiles of the high-Pb films exhibit initial increases followed by decreases, qualitatively replicating the trend of the broadband FWHM in these films. Overall, the characteristics in time-evolved PL spectra of the films obviously suggest that phase segregation is the major factor in broadband emission in compositions with higher Pb ratios in the mixed Pb-Sn 2D MHPs.

To gain insights into the chemical structures of the elements, particularly the emergence of defects, across the compositional space in mixed Pb-Sn 2D MHP system, X-ray photoelectron spectroscopy (XPS) is conducted on the thin films and the Sn *3d*, Pb *4f*, and I *3d* core-level photoelectron emission spectra of the films are collected. The baseline-subtracted Sn *3d* XPS spectra are shown in Figure S12a (Supporting Information). Two distinctive peaks centered at ≈484.5 and 486 eV, assigned to be metallic Sn (Sn^0) and Sn^{2+}, respectively,[35] are observed from the Sn $3d_{5/2}$ spectra in the overall compositional range except for pure PEA_2SnI_4. The peaks at ≈486 eV show asymmetric features attributed to the defective Sn^{4+} component centered at ≈487 eV. This is widely observed in Sn-based perovskite because of the susceptibility of Sn^{2+} upon oxidation.[35] While the lattice-occupying Sn^{2+} peak proportionally becomes weaker with increasing Pb composition ratios, Sn^0 peak – known to also promote non-radiative recombination as defect[36] – substantially evolves and increases to the comparable intensity with that of Sn^{2+}. To get quantified insights into the Sn chemistry in 2D Pb-Sn MHPs, the Sn $3d_{5/2}$ spectra are deconvoluted into three distinct components corresponding to Sn^{4+}, Sn^{2+}, and Sn^0, respectively, as

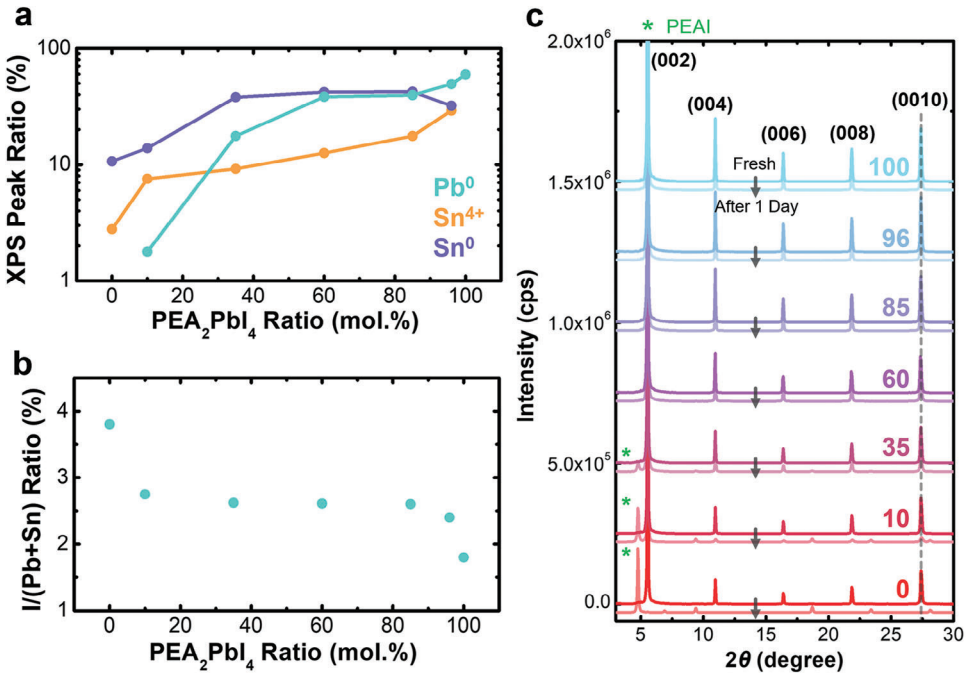

Figure 3. a) Relative ratios of Pb^0, Sn^{4+}, and Sn^0 with respect to total atomic contents. b) Estimated I/(Pb+Sn) ratios of the 2D MHP films with different Pb ratios derived from the deconvolution of the corresponding XPS spectra. c) XRD patterns of the freshly prepared 2D MHP films with different Pb ratios and those were left in ambient for one day. The green asterisks indicate the diffraction peak of PEAI.

shown in Figure S12b (Supporting Information) (detailed values are summarized in Table S1, Supporting Information). Obviously, in addition to Sn^0, it is observed that Sn^{4+} component gradually evolves with increasing Pb composition ratio (**Figure 3a**). Note that the films are carefully transferred to ultra-high vacuum (UHV) chamber for measurement with a minimized exposure to ambient conditions, as corroborated by the nearly exclusive emergence of Sn^{2+} peak in the XPS Sn *3d* spectrum of pure PEA_2SnI_4 film.

Similarly, strong metallic Pb (Pb^0) peak – centered at ≈136.5 eV in Pb $4f_{7/2}$ region – and the lattice-occupying Pb^{2+} peak (≈137.8 eV in Pb $4f_{7/2}$ region) are observed in Pb *4f* XPS spectra,[37] where the former component increases with increasing Pb composition ratio in Pb *4f* XPS spectra (Figure S13a, Supporting Information). The quantitative trend after peak deconvolution (see Figure S13b and Table S1, Supporting Information) is also visualized in Figure 3a, clearly showing a progressive increase of Pb^0 defects with increasing Pb ratio in the 2D MHP films. In contrast to PEA_2SnI_4, pure PEA_2PbI_4 film exhibits the strongest Pb^0 peak, suggesting that the origin of Sn^0 in mixed Pb-Sn MHPs is associated with the chemical action of Pb. Accordingly, exposure of Pb-based MHPs to UHV conditions and X-ray photon irradiation can cause iodine evaporation as a form of I_2 gas,[35] thereby promoting Pb^{2+} to Pb^0 reduction.[38] In mixed Pb-Sn 2D MHP, this reducing action – initiated from Pb-I part – can also affect neighboring Sn^{2+} in the lattice, thereby producing Sn^0.

We further analyzed the I 3d spectra across all films to understand the nuanced changes in binding energy associated with varying lead concentrations. Figure S14 (Supporting Information) shows I *3d* spectra of the 2D MHP films, exhibiting serial upshifts in binding energy up to ≈0.2 eV with increasing Pb ratio. In fact, stronger interaction between Sn and I compared with the Pb counterpart is deemed to result in binding energy downshift with increasing Pb ratio, which is inconsistent with the observations. Such contradictory results infer that other factors are likely associated with the spectral feature. We estimated the I/(Pb+Sn) ratio of the films (Figure 3b; and Table S1, Supporting Information),[39] showing a drop in I concentration in the 2D MHP matrix with increasing Pb ratio. While the elucidation of the exact origin of metallic Pb and Sn in 2D Pb-Sn HPs remains uncertain and out of the scope of this work, the magnitude of I/(Pb+Sn) changes and the associated peak shifts across the composition ratios are relatively minor. In contrast, the sequential changes observed in the Sn 3d and Pb 4f spectra are markedly distinctive. This suggests that iodine vacancies are not significantly affected by such extreme experimental conditions (UHV or X-ray-induced damaging). That is, relatively higher amounts of I vacancies are formed in the film with increasing Pb ratios – particularly in high-Pb films – which is likely responsible for the upshifts in I 3d spectra. Note that among various defects, I vacancy, particularly that in equatorial position rather than in apical position, is known to be responsible for local trapping of charge carrier and the consequent peak broadening in 2D Pb-Sn MHPs.[9b] XPS results indicate that, both mechanisms respectively associated with defects and phase segregation contribute to the widening of FWHM of the broad emission, where the impact of the latter mechanism becomes more pronounced with increasing Pb contents.

Through ultraviolet photoelectron spectroscopy (UPS) analysis, we observe distinctive changes in electronic structures of mixed Pb-Sn 2D MHPs as a function of Pb composition ratios (Figure S15, Supporting Information). Here, a low-energy

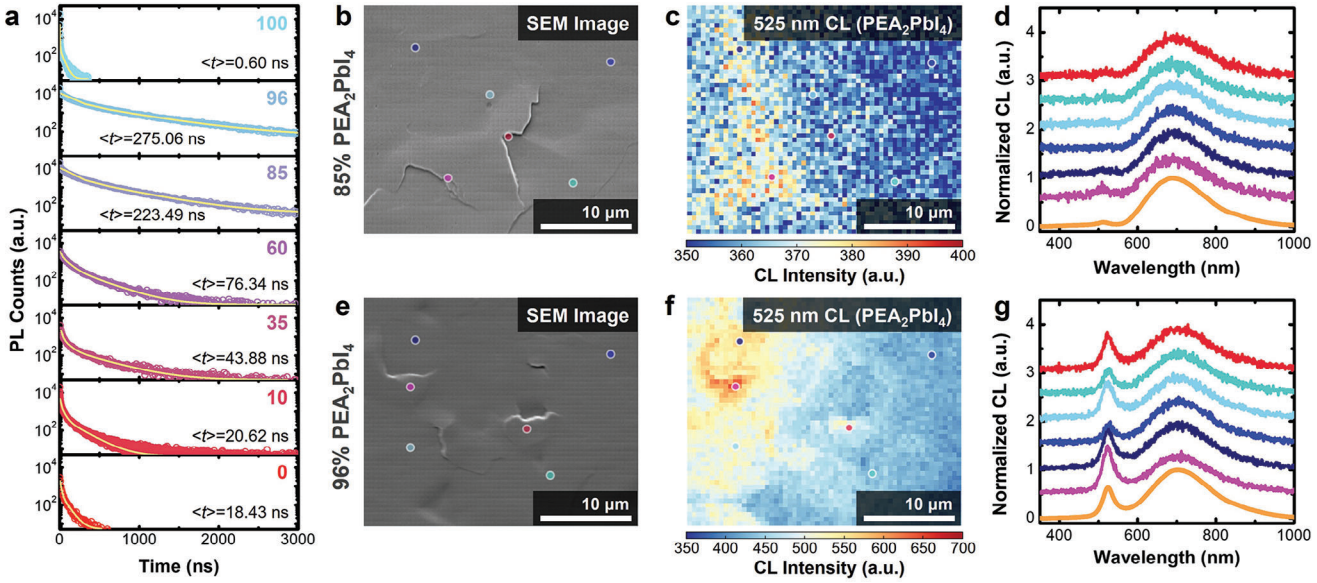

Figure 4. a) PL decays and calculated average lifetimes collected from 2D MHP films with increasing Pb ratios. b,e) SEM images, c,f) 525 nm-filtered CL maps (assigned to PEA_2PbI_4), and d,g) local CL spectra of six spots color-marked on the maps for the films with 85 and 96% PEA_2PbI_4, respectively.

incidence photon of 10.2 eV was used as a UV source to mitigate the beam-induced damage, particularly on the organic part during experiments.[40] Based on the extracted Fermi energy (E_F) and valence band maximum (E_V) – respectively calculated from the secondary electron cut-off and valence band spectral regions (Figures S16 and S17, Supporting Information) – and E_g of mixed-phases calculated from Tauc plots (Figure S10, Supporting Information), the energy level diagram of the 2D MHP films are reconstructed (Figure S18, Supporting Information). Overall, the E_F upshifts away from the valence band edge towards the middle of the E_g, indicating less p-type doping, are observed with increasing the Pb ratios, which aligns with the self p-doped nature of Sn rich MHPs.[41] The notable separation of the less p-typed PEA_2PbI_4 from the mixed Pb-Sn phases is likely reflected in the notable jump of E_F-E_V (from 0.67 to 0.84–0.89 eV) in the films with 85, 96, and 100% Pb. Also, the higher densities of iodine vacancies as evidenced in XPS analysis, which is known to facilitate a shift towards a more n-type surface character in 3D MHP[42] – could be also associated with this jump. Summarizing, the interplay of self p-doping properties of Sn^{2+}, notable phase separation, and higher densities of iodine vacancy synergistically bestow mediated p-type character to the films with increasing Pb ratios.

Defects are known to sacrifice the stability of MHPs, suspecting that Pb-rich 2D Pb-Sn MHPs are more susceptible to degradation. To explore the influence of defects identified in XPS analysis on the stability of 2D MHP films, X-ray Diffraction (XRD) patterns of both the freshly prepared samples and those that were left in the ambient environment for a day are collected (Figure 3c). All films exhibit distinctive diffraction patterns of 2D MHPs with strong fundamental peaks at ≈5.40°, assigned to be (002) face-on oriented lattice stacking mode.[16] After a day in ambient conditions, the intensity drop of 2D MHP diffraction peaks as well as the emergence of a new peak ≈4.8° (marked with green asterisks; assigned to be PEAI[22,43]) that shows stronger intensity with decreasing Pb ratios are observed. This indicates the 2D MHP crystallites, particularly the inorganic lattices are disintegrated upon ambient degradation. Note that the degradation is more facilitated in the film with decreasing Pb ratios due to the chemical lability of Sn^{2+} upon oxidation. Zoom-in XRD patterns of the (0010) planes for both fresh and degraded samples are displayed in Figure S19 (Supporting Information) and the FWHM and intensity of the XRD peaks were quantified from fitted results. The peak intensity increases with higher Pb concentrations for fresh samples, indicating enhanced crystallinity associated with them. Conversely, while peak intensity increases in degraded samples with higher Pb content, the FWHM decreases, suggesting larger crystallite sizes according to the Scherrer equation.[44] Moreover, despite all films demonstrating good crystallinity, no peak splitting related to phase segregation is observed. This absence of peak splitting can be attributed to the limitation of XRD in detecting subtle lattice modifications, including phase separations, particularly in complex systems.[45]

To further investigate the role of defects on the PL characteristics, time-resolved PL decays of the 2D MHP films are measured using a sub-bandgap excitation wavelength of 1027 nm, as shown in **Figure** 4a. Here, as the photon energies below the bandgap lack the capacity to directly excite the carriers to the band edge, the broadband emission under this condition effectively negates the STE emission scenario.[25,46] To explore whether STEs underlie the broad emission, the PL spectra of the films were collected using above and below-bandgap excitation wavelengths of 365 and 650 nm, respectively (Figure S20, Supporting Information). Interestingly, the PL spectra of the films – particularly with high Pb ratios – collected with 650 nm excitation are broader than those from 365 nm excitation. While the above-bandgap excitation triggers STE emission producing broadband PL, the emission from CTE – exclusively promoted by sub-bandgap excitation – results in much wider broadband PL beyond STE can solely manifest. This indicates CTE is more responsible for the much broader PL emission. In Figure 4a, while pure 2D MHPs exhibit

very fast PL decays, interestingly, the mixed Pb-Sn MHPs exhibit slower decays, which are further prolonged with increasing Pb ratios. By employing a triexponential peak fitting model, the average lifetime is calculated for each sample (see Table S2, Supporting Information). The pure 2D endmembers exhibit short lifetimes of 18 and 0.6 ns for PEA_2SnI_4 and PEA_2PbI_4, respectively, in good agreement with previous studies.[15a,16] Serial increases in PL lifetime from 20.62 to 275.06 ns are observed from the mixed Pb-Sn 2D MHPs with increasing Pb ratios, even though the defects (i.e., iodine vacancies) become higher in the films in XPS observations.[47] Such a contradictory trend suggests that the CTE states established by the interfacial contacts between the segregated PEA_2PbI_4 and the mixed Pb-Sn 2D HPs – rather than increased defects (I vacancy) – are responsible for higher PL lifetime of samples with higher Pb content.[16] Furthermore, we utilized TRPL with pulsed excitation wavelengths above the bandgap, specifically at 343 nm. The results, as depicted in Figure S21 (Supporting Information) (and Table S3, Supporting Information), clearly show that the lifetimes of these samples follow the same trend as Figure 4a. However, it is noteworthy that the lifetimes observed with above-bandgap excitation (343 nm) are shorter than those with sub-bandgap excitation (1027 nm). While the sub-bandgap photons can exclusively excite the charges to CTE states, the above-bandgap photons can populate all possible excitonic states with different physical origins. For the latter scenario, the relative portion of the CTE-originated excitons in the radiative relaxation process, which is associated with the broadband PL, decreases. Additionally, the observed increase in lifetime with higher excitation wavelengths suggests that the measurements predominantly occur within the radiative regime. This effectively minimizes high-order charge carrier recombination processes, such as Auger recombination[48] and exciton-exciton annihilation,[49] ensuring that the laser settings are optimized to emphasize radiative transitions over non-radiative losses. Note that the observed PL lifetimes of our polycrystalline films are longer than those collected from Sn-doped PEA_2PbI_4 single crystal,[23] where the evolution of the interface between the segregated phases is minimized and thus majorly renders PL from STEs. This suggests that the emergence of other PL components responsible for broadband PL – activated by above-bandgap excitation – can reduce the overall lifetime of broadband PL. These findings compellingly indicate that the phase segregation of mixed Pb:Sn phases plays a key role in the broadening of PL peaks.

Finally, to gain spatially resolved insights into the mixed Pb-Sn 2D MHPs, hyperspectral cathodoluminescence (CL) microscopy is employed for several selected Pb-Sn thin films.[21,50] For pure PEA_2SnI_4 and PEA_2PbI_4 films, distinctive band-edge emissions (as visualized in 625 and 525 nm-filtered CL maps, respectively) of the films are observed across the entire surface with slight local intensity contrasts (Figure S22, Supporting Information). This suggests that those films possess imperfect chemical homogeneity in the respective lattice interiors, likely attributed to the defects. Note that, in contrast to PEA_2PbI_4, substantial amounts of small voids are observed on the PEA_2SnI_4 surface. This could be explained by the extreme susceptibility of Sn^{2+}-based lattice upon ambient oxidation that leads to degradation,[51] which however does not compromise the spectral shape of emission characteristics. In other words, while the oxidation process leads to the formation of Sn^{4+} species, which impacts the structure of the films, it does not significantly affect the broadband PL features.

For the mixed 2D Pb-Sn MHP films with low Pb ratios (i.e., 10, 35, and 60% PEA_2PbI_4), such voids are not observed on the surfaces, suggesting the oxidative degradation action is somewhat mitigated upon Pb incorporation (Figure S23, Supporting Information). Also, in both 625 and 700 nm-filtered CL maps – corresponding with the peak and shoulder of the broadband spectra, broadband CL peak is observed across the entire film surface. Stronger CL intensities are observed along the grain boundaries, which could be attributed to the higher charge density at the edge of the 2D MHPs[52] that constitutes the grain boundaries. Specifically for the film with 35% PEA_2PbI_4, two spots within 500 nm pixel size emitting asymmetric CL emission centered ≈388 nm are identified (Figure S24, Supporting Information). This is likely attributed to the formation of SnO_2 particles as a product of Sn^{2+} to Sn^{4+} oxidation.[53] Note that these spots are observed at the grain boundaries, suggesting that the oxidation action directly through the PEA-coordinated 2D faces is mitigated upon Pb incorporation and thereby exclusively occurring at the reactive surface spots. Moreover, despite this clear indication of Sn oxidation in the CL data, UV–vis absorption spectra of these samples (i.e., films with high-Sn concentrations) do not exhibit any peaks attributable to oxidation of Sn (Figure S10, Supporting Information). This absence suggests that the oxidation of Sn does not significantly alter the absorption characteristics of these films.

Figure 4b,e exhibits SEM images of mixed Pb-Sn 2D MHPs with high Pb ratios of 85 and 96%, respectively, showing nominal surface morphologies with flattened surfaces observed in the other films. Seven hundred nanometers-filtered CL maps of the film also exhibit no specific spatial contrast in broadband emissions (Figure S25, Supporting Information). However, 525 nm-filtered maps – responsible for PEA_2PbI_4 – clearly show non-zero CL intensity with distinctive local contrasts in these film surfaces, which exhibits the strongest intensities at the grain boundaries and then propagates towards the surroundings (Figure 4c,f). This suggests that the PEA_2PbI_4 phase starts to segregate from the defective grain boundaries upon film crystallization and exhibits long-range coverage to the entire film surface. Atomic Force Microscopy (AFM) images of the films present in Figure S26 (Supporting Information) illustrate that an increase in Pb content correlates with a reduction in grain size, indicative of more prominent grain boundaries within these compositions. The emergence of the segregated PEA_2PbI_4 phase is also evident in the corresponding local CL spectra (Figure 4d,g). Based on the results, we conclude that the interfacial contact between the segregated PEA_2PbI_4 lattice and the mixed Pb-Sn 2D MHP lattice effectively establishes CTE states across the entire film surface, thus majorly contributing to the long-lived broadband emission.[16]

In fact, defects – particularly the iodine vacancy – have been claimed to promote peak widenings in broadband emission stemming from Stokes-shift (**Figure** 5a,d,e), which have been experimentally observed in PL spectra of the pure 2D MHPs collected at cryogenic temperatures.[9b,14b,15] This model can be expanded to the observations in 2D MHPs with low-Pb ratios, which shows a nominal level of the broadband FWHM but no appreciable segregated PEA_2PbI_4 phase (Figure 5b,f). In this study, clearly, the emergence of PEA_2PbI_4 phase in the mixed

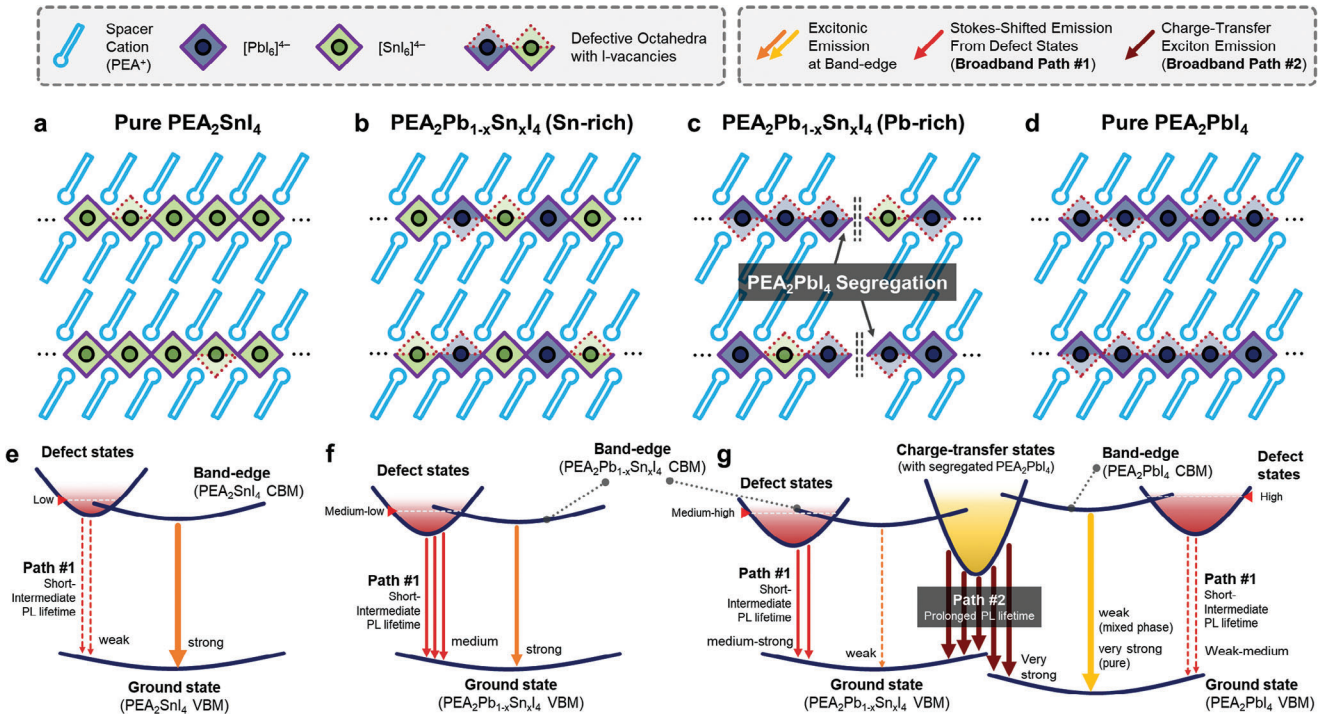

Figure 5. a–d) Schematics describing lattice structures in 2D Pb-Sn MHPs and e–g) corresponding Jablonski diagrams explaining broadband emission mechanisms at respective composition ranges.

Pb-Sn 2D MHP is spatially resolved, which reveals that the segregation action starts to occur at the grain boundaries that are deemed to possess larger amounts of defects. As hypothesized from the high-throughput observations, the incompatible crystallization kinetics with different chemical natures of Sn and Pb-based 2D MHPs could be mainly responsible for the formation of defects during the initial stage of crystallization of the solution-processed films. These defects, rather than inducing spectral Stokes-shift, in turn, can simultaneously promote the segregation of PEA_2PbI_4 during the rest of the crystallization process. As a result, the "unexpected" interfacial contacts between PEA_2PbI_4 and the mixed Pb-Sn 2D MHPs establish the CTE states for broadband emission (Figure 5c,g). We stress that high-throughput exploration provides indispensable and comprehensive insights into the detailed crystallization dynamics that cannot easily be captured in conventional experimental workflow, significantly accelerating the discovery of the genuine origin of the fundamental material's properties. This work exemplifies how high-throughput automated experimental workflow sheds light on the fundamental discovery of functional materials. In fact, these observations emphasize the intricate relationship between composition, degradation, and photophysical properties in mixed 2D Pb-Sn HPs, shedding light on how compositional variations influence the optical characteristics of these materials.

3. Conclusion

In summary, the early-stage crystallization dynamics of mixed Pb-Sn 2D MHPs are investigated by implementing high-throughput automated experimental workflow to explore the broadband PL emission of this materials system. This significantly accelerates the quantitative and comprehensive understanding of relationship between the broadband emission and crystallization behaviors, which has not been deeply considered so far. It is revealed that the broadband emission exhibits a strong correlation with the segregation of PEA_2PbI_4 that is facilitated at high-Pb compositional ratios, hypothesizing that the establishment of CTEs, alongside defects, are mainly responsible for the broadband emission. This is attributed to the incompatible crystallization kinetics and different chemical nature between Sn and Pb-based 2D MHPs, bestowing nontrivial chemical complexity in the film crystallites. XPS characterizations reveal that the iodine vacancies progressively evolve with increasing Pb ratios – exclusively responsible for sub-bandgap states inducing Stokes-shift, remains insignificant variation across the mixed Pb-Sn compositional space. Hyperspectral CL microscopy reveals that substantial segregation of PEA_2PbI_4 phases in the mixed Pb-Sn 2D MHP films particularly with high-Pb ratios indeed, the evolution of which is initiated from the defective grain boundaries. Thus, we conclude that the evolution of prolonged broadband PL originated from the coexistence of defects and the establishment of CTE by phase segregation. This effectively reconciles the proposed models describing the fundamental origin of broadband emissions, which are in debate. Elucidation of the genuine origin of these fundamental properties of promising materials sheds light on the development of sustainable and ubiquitous applications. More importantly, this study evidently exemplifies how the fundamental properties in chemically complex materials can be comprehensively explored and discovered in an accelerated manner via unconventional high-throughput automated experimental workflow.

4. Experimental Section

Materials: Phenethylammonium iodide (PEAI; Sigma-Aldrich, 98%), Tin(II) iodide (SnI2; Sigma-Aldrich, 99.99%), lead (II) iodide (PbI2; Fisher Scientific, 99.99% ultra-dry, metals basis), N,N-dimethylformamide (DMF; Sigma-Aldrich, 99.8% anhydrous), Dimethylsulfoxide (DMSO; Sigma-Aldrich, ≥99.9% anhydrous), γ-butyrolactone (GBL; Sigma-Aldrich, ≥99%), and toluene (Sigma-Aldrich, 99.8% anhydrous) were purchased and used without further purification.

High-Throughput Robotic Synthesis of 2D MHP Microcrystals: To prepare precursor solutions, stoichiometric amounts of $PEAI_2PbI_4$ and $PEAI_2SnI_4$ precursor solutions (0.3 M) were dissolved in GBL in an N_2 glovebox and stirred for 5 h at room temperature. Then the solutions were transferred to the pipetting robot system with the N_2 atmosphere. Fifty microliters of precursor solutions with 96 different Pb-Sn composition ratios were filled into each well of a microplate using a pipetting robot (Opentrons, OT-2) by combinatorial mixing of both precursor solutions as endmembers (Figure S1, Supporting Information). By injecting 250 µL of toluene (as an antisolvent) into each well, a microplate with microcrystals having target Pb-Sn composition ratios were synthesized automatically. The high-throughput robotic system operates entirely within an N_2-filled enclosure, where both humidity and temperature were closely monitored and recorded for each experiment, before and during synthesis. For this specific experiment, the humidity was maintained at 0.5% RH at a temperature of 24 °C.

Photoluminescence Measurements: After synthesis, the well plate was immediately sealed with a 96-well plate sealing film while still within the controlled environment of the robot. This prompt sealing minimizes any exposure to external environmental factors. The sealed plate was then quickly transferred to the hybrid multi-mode optical reader (BioTek, Cytation 5), located close to the robotic system. Then the PL spectra (1 nm step) were collected from each well over time. The excitation wavelength was 405 nm. A "read" cycle was used to collect 96 spectra from each well every 10 min, which was repeated over 100 cycles (1000 min) to get time-evolved PL spectra. This means that the well plate remains in the reader for that entire duration without any interruptions. Initially, the reader collects the PL spectra of all 96 compositions in the well plate. In subsequent reads, the reader measures the PL spectra of all compositions again and repeats this process over the 16 h. This method ensures that the time conditions for PL measuring were consistent for all compositions with different Pb:Sn ratios, allowing for a reliable comparison and thorough analysis of the photoluminescence properties across the entire sample set. Data analysis was performed on Google Colab using Python 3.6. The code is available in the following link (Google Colab): https://colab.research.google.com/drive/1x1RTuQuNX6Z6rI98fMmPi86jK5yYGxnr?usp=drive_link.

Thin Film Synthesis: Stoichiometric amounts of PEA_2PbI_4 and PEA_2SnI_4 precursor solutions were dissolved in a mixed solvent of anhydrous DMF:DMSO with a volume ratio of 4:1. PL spectra of several selected Pb:Sn thin films with two different solvents, DMF and DMF:DMSO, reveal that the mixed solvent results in higher PL intensity and reduced phase segregation, as observed in Figure S7 (Supporting Information). Thin films were cast on glass substrates, and they were ultrasonically cleaned in deionized water, isopropanol, and acetone, respectively. After drying substrates with N_2, they were treated with ultraviolet ozone for 20 min and immediately transferred into the N_2 glovebox for film deposition. The fabrication of the films involved a two-step spin coating process, 1000 rpm for 10 s, followed by 5000 rpm for 40 s. Then, the films were annealed at 100 °C for 10 min. PL spectra of several selected Pb:Sn thin films annealed at two different temperatures are presented in Figure S8 (Supporting Information), demonstrating higher intensity with an annealing temperature of 100 °C.

Characterizations: Using the same optical reader as for PL measurements, the films' absorption spectra were measured. Data analysis was performed on Google Colab using Python 3.6. The code is available in the following link (Google Colab): https://colab.research.google.com/drive/1IvF4Xo_hrykBiTlfHxbu99kgK9ADdvzB?usp=drive_link. XPS measurements were performed with a Scienta Omicron XPS Lab instrument using a monochromated Al Kα anode (1486 eV). For the UPS measurements, the H Lyman-photon source (E-LUX 121) used had a photon energy of 10.2 eV and a pass energy of 5.85 eV, and the sample was biased at a potential of −5 V. TRPL decays were measured by using a Horiba Fluorolog 3 spectrometer and PPD-900 photon counting detector. A setup was utilized with multiple laser excitation capabilities, specifically at wavelengths of 343 and 1027 nm. The power densities for these wavelengths were measured at ≈80 and 1200 µJ cm^{-2}, respectively. These values were determined using a power meter to directly measure the laser's power output, which was then divided by the area of the laser spot to calculate the power density. The filtered harmonics of the excitation sources were generated from a 280 fs pulsed laser operating at 50 kHz. XRD patterns of the films were acquired by using a high-resolution X-ray diffractometer (Malvern Panalytical, Empyrean). Hyperspectral CL microscopy data were collected by using an environmental SEM instrument (FEI, Quattro) with a Delmic Sparc CL collection module. A parabolic mirror was utilized to collect the CL signals upon e-beam excitation. An e-beam with an acceleration voltage of 5 kV (beam current of 28 pA) with a dynamic acquisition time ranging 500–1000 ms was used for CL measurements. The pixel size was fixed to 500 × 500 nm^2. All measurements were conducted in a low vacuum environment of 0.02 Torr with H_2O vapor, which effectively alleviated sample charging while minimizing electron-beam-induced damage.

Supporting Information

Supporting Information is available from the Wiley Online Library or from the author.

Acknowledgements

E.F., J.Y., and M.A. acknowledge support from National Science Foundation (NSF), Award Number 2043205, and Alfred P. Sloan Foundation, award No. FG-2022-18275. The XPS and CL experiments were supported by the Center for Nanophase Materials Sciences (CNMS), which is a US Department of Energy, Office of Science User Facility at Oak Ridge National Laboratory. S.J. and K.R.G. performed the UPS measurements and acknowledged support from the National Science Foundation under cooperative agreement No. 1849213.

Conflict of Interest

The authors declare no conflict of interest.

Data Availability Statement

The data that support the findings of this study are available in the supplementary material of this article.

Keywords

2D Pb-Sn halide perovskites, broad emissions, high-throughput experiments, phase segregations

Received: June 25, 2024
Revised: July 30, 2024
Published online: August 24, 2024

[1] a) J. Huang, Y. Yuan, Y. Shao, Y. Yan, *Nat. Rev. Mater.* **2017**, *2*, 17042; b) J. Luo, R. He, H. Lai, C. Chen, J. Zhu, Y. Xu, F. Yao, T. Ma, Y. Luo, Z. Yi, Y. Jiang, Z. Gao, J. Wang, W. Wang, H. Huang, Y. Wang, S. Ren, Q. Lin, C. Wang, F. Fu, D. Zhao, *Adv. Mater.* **2023**, *35*, 2300352.

[2] C. Liang, H. Gu, Y. Xia, Z. Wang, X. Liu, J. Xia, S. Zuo, Y. Hu, X. Gao, W. Hui, *Nat. Energy* **2021**, *6*, 38.
[3] H. Tsai, W. Nie, J. C. Blancon, C. C. Stoumpos, C. M. M. Soe, J. Yoo, J. Crochet, S. Tretiak, J. Even, A. Sadhanala, *Adv. Mater.* **2018**, *30*, 1704217.
[4] a) T. L. Leung, I. Ahmad, A. A. Syed, A. M. C. Ng, J. Popović, A. B. Djurišić, *Commun. Mater.* **2022**, *3*, 63; b) X. Li, J. M. Hoffman, M. G. Kanatzidis, *Chem. Rev.* **2021**, *121*, 2230.
[5] a) C. Deng, G. Zhou, D. Chen, J. Zhao, Y. Wang, Q. Liu, *J. Phys. Chem. Lett.* **2020**, *11*, 2934; b) L. Mao, H. Tsai, W. Nie, L. Ma, J. Im, C. C. Stoumpos, C. D. Malliakas, F. Hao, M. R. Wasielewski, A. D. Mohite, M. G. Kanatzidis, *Chem. Mater.* **2016**, *28*, 7781; c) X. Wu, M. T. Trinh, X. Y. Zhu, *J. Phys. Chem. C* **2015**, *119*, 14714.
[6] a) A. Abate, *Joule* **2017**, *1*, 659; b) J. Xi, M. A. Loi, *ACS Energy Lett.* **2021**, *6*, 1803.
[7] J. Yang, W. Han, B. Jiang, C. Wang, Y. Sun, H. Zhang, K. Shimanoe, P. Sun, G. Lu, *Sens. Actuators, B* **2023**, *387*, 133801.
[8] B. Mulyani, A. S. F. B. Manullang, A. D. Purwanti, R. F. Anisa, *AIP Conf. Proc.* **2023**, *2540*, 050012.
[9] a) F. Hao, C. C. Stoumpos, R. P. Chang, M. G. Kanatzidis, *J. Am. Chem. Soc.* **2014**, *136*, 8094; b) S. Kahmann, D. Meggiolaro, L. Gregori, E. K. Tekelenburg, M. Pitaro, S. D. Stranks, F. De Angelis, M. A. Loi, *ACS Energy Lett.* **2022**, *7*, 4232.
[10] H. Yao, F. Zhou, Z. Li, Z. Ci, L. Ding, Z. Jin, *Adv. Sci.* **2020**, *7*, 1903540.
[11] J. Cao, F. Yan, *Energy Environ. Sci.* **2021**, *14*, 1286.
[12] a) A. Ray, L. De Trizio, J. Zito, I. Infante, L. Manna, A. L. Abdelhady, *Adv. Opt. Mater.* **2023**, *11*, 2202005; b) J. Zhao, Z. Zhang, G. Li, M. H. Aldamasy, M. Li, A. Abate, *Adv. Energy Mater.* **2023**, *13*, 2204233.
[13] a) S. Kahmann, E. K. Tekelenburg, H. Duim, M. E. Kamminga, M. A. Loi, *Nat. Commun.* **2020**, *11*, 2344; b) B. M. Benin, D. N. Dirin, V. Morad, M. Worle, S. Yakunin, G. Raino, O. Nazarenko, M. Fischer, I. Infante, M. V. Kovalenko, *Angew. Chem., Int. Ed.* **2018**, *57*, 11329; c) L. Mao, P. Guo, M. Kepenekian, I. Hadar, C. Katan, J. Even, R. D. Schaller, C. C. Stoumpos, M. G. Kanatzidis, *J. Am. Chem. Soc.* **2018**, *140*, 13078; d) L. Mao, Y. Wu, C. C. Stoumpos, M. R. Wasielewski, M. G. Kanatzidis, *J. Am. Chem. Soc.* **2017**, *139*, 5210.
[14] a) J. Li, H. Wang, D. Li, *Front. Optoelectron.* **2020**, *13*, 225; b) W. Paritmongkol, E. R. Powers, N. S. Dahod, W. A. Tisdale, *J. Phys. Chem. Lett.* **2020**, *11*, 8565.
[15] a) H. H. Fang, E. K. Tekelenburg, H. Xue, S. Kahmann, L. Chen, S. Adjokatse, G. Brocks, S. Tao, M. A. Loi, *Adv. Opt. Mater.* **2023**, *11*, 2202038; b) H. Hu, Y. Liu, Z. Xie, Z. Xiao, G. Niu, J. Tang, *Adv. Opt. Mater.* **2021**, *9*, 2101423.
[16] J. Zhang, X. Zhu, M. Wang, B. Hu, *Nat. Commun.* **2020**, *11*, 2618.
[17] C. Zhang, J. Lin, *Chem. Soc. Rev.* **2012**, *41*, 7938.
[18] M. D. Smith, H. I. Karunadasa, *Acc. Chem. Res.* **2018**, *51*, 619.
[19] a) J. Yang, B. J. Lawrie, S. V. Kalinin, M. Ahmadi, *Adv. Energy Mater.* **2023**, *13*, 2302337; b) S. L. Sanchez, Y. Tang, B. Hu, J. Yang, M. Ahmadi, *Matter* **2023**, *6*, 2900; c) K. Higgins, S. M. Valleti, M. Ziatdinov, S. V. Kalinin, M. Ahmadi, *ACS Energy Lett.* **2020**, *5*, 3426; d) K. Higgins, M. Ziatdinov, S. V. Kalinin, M. Ahmadi, *J. Am. Chem. Soc.* **2021**, *143*, 19945.
[20] H. Hysmith, E. Foadian, S. P. Padhy, S. V. Kalinin, R. G. Moore, O. S. Ovchinnikova, M. Ahmadi, *Digital Discovery* **2024**, *3*, 621.
[21] J. Yang, D. K. LaFollette, B. J. Lawrie, A. V. Ievlev, Y. Liu, K. P. Kelley, S. V. Kalinin, J.-P. Correa-Baena, M. Ahmadi, *Adv. Energy Mater.* **2023**, *13*, 2202880.
[22] Y. Ju, X. g. Wu, S. Huang, G. Dai, T. Song, H. Zhong, *Adv. Funct. Mater.* **2022**, *32*, 2108296.
[23] J. Yu, J. Kong, W. Hao, X. Guo, H. He, W. R. Leow, Z. Liu, P. Cai, G. Qian, S. Li, *Adv. Mater.* **2019**, *31*, 1806385.
[24] a) Y. Chen, Y. Sun, J. Peng, P. Chábera, A. Honarfar, K. Zheng, Z. Liang, *ACS Appl. Mater. Interfaces* **2018**, *10*, 21343; b) M. Wei, K. Xiao, G. Walters, R. Lin, Y. Zhao, M. I. Saidaminov, P. Todorović, A. Johnston, Z. Huang, H. Chen, *Adv. Mater.* **2020**, *32*, 1907058; c) Z. Wang, Q. Ou, Y. Zhang, Q. Zhang, H. Y. Hoh, Q. Bao, *ACS Appl. Mater. Interfaces* **2018**, *10*, 24258.
[25] T. Li, X. Chen, X. Wang, H. Lu, Y. Yan, M. C. Beard, D. B. Mitzi, *ACS Energy Lett.* **2019**, *5*, 347.
[26] a) M. A. Smith, M. Chen, Z. Dai, C. Antolini, G. K. Jayasekara, S. K. Yadavalli, B. J. Reinhart, N. P. Padture, D. Hayes, *ACS Appl. Energy Mater.* **2021**, *4*, 4327; b) Y.-H. Cheng, R. Moriyama, H. Ebe, K. Mizuguchi, R. Yamakado, S. Nishitsuji, T. Chiba, J. Kido, *ACS Appl. Mater. Interfaces* **2022**, *14*, 22941.
[27] a) F. Barry, V. Cunnane, *J. Electroanal. Chem.* **2002**, *537*, 151; b) H. Wang, M. Pritzker, *Electrochim. Acta* **2008**, *53*, 2430.
[28] G. Vescio, J. Sanchez-Diaz, J. L. Frieiro, R. S. Sanchez, S. Hernandez, A. Cirera, I. Mora-Sero, B. Garrido, *ACS Energy Lett.* **2022**, *7*, 3653.
[29] a) F. Zhang, D. H. Kim, H. Lu, J.-S. Park, B. W. Larson, J. Hu, L. Gao, C. Xiao, O. G. Reid, X. Chen, *J. Am. Chem. Soc.* **2019**, *141*, 5972; b) M. M. Abdelhamied, Y. Gao, X. Li, W. Liu, *Appl. Phys. A* **2022**, *128*, 57.
[30] C. Wang, S. Cui, Y. Ju, Y. Chen, S. Chang, H. Zhong, *Adv. Funct. Mater.* **2023**, *33*, 2301304.
[31] a) C. C. Underwood, J. D. Carey, S. R. P. Silva, *J. Phys. Chem. Lett.* **2021**, *12*, 1501; b) G. E. Eperon, T. Leijtens, K. A. Bush, R. Prasanna, T. Green, J. T.-W. Wang, D. P. McMeekin, G. Volonakis, R. L. Milot, R. May, *Science* **2016**, *354*, 861.
[32] F. Urbach, *Phys. Rev.* **1953**, *92*, 1324.
[33] a) A. Sadhanala, F. Deschler, T. H. Thomas, S. E. Dutton, K. C. Goedel, F. C. Hanusch, M. L. Lai, U. Steiner, T. Bein, P. Docampo, *J. Phys. Chem. Lett.* **2014**, *5*, 2501; b) G. Cody, T. Tiedje, B. Abeles, B. Brooks, Y. Goldstein, *Phys. Rev. Lett.* **1981**, *47*, 1480.
[34] a) H. H. Fang, J. Yang, S. Tao, S. Adjokatse, M. E. Kamminga, J. Ye, G. R. Blake, J. Even, M. A. Loi, *Adv. Funct. Mater.* **2018**, *28*, 1800305; b) J.-W. Lee, Z. Dai, T.-H. Han, C. Choi, S.-Y. Chang, S.-J. Lee, N. De Marco, H. Zhao, P. Sun, Y. Huang, *Nat. Commun.* **2018**, *9*, 3021.
[35] a) A. Wieczorek, H. Lai, J. Pious, F. Fu, S. Siol, *Adv. Mater. Interfaces* **2023**, *10*, 2201828; b) K. W. Yeom, D. K. Lee, N. G. Park, *Adv. Energy Mater.* **2022**, *12*, 2202496; c) R. Lin, J. Xu, M. Wei, Y. Wang, Z. Qin, Z. Liu, J. Wu, K. Xiao, B. Chen, S. M. Park, *Nature* **2022**, *603*, 73.
[36] T. B. Song, T. Yokoyama, C. C. Stoumpos, J. Logsdon, D. H. Cao, M. R. Wasielewski, S. Aramaki, M. G. Kanatzidis, *J. Am. Chem. Soc.* **2017**, *139*, 836.
[37] a) D. Bi, C. Yi, J. Luo, J.-D. Décoppet, F. Zhang, S. M. Zakeeruddin, X. Li, A. Hagfeldt, M. Grätzel, *Nat. Energy* **2016**, *1*, 16142; b) J. Zhuang, P. Mao, Y. Luan, X. Yi, Z. Tu, Y. Zhang, Y. Yi, Y. Wei, N. Chen, T. Lin, *ACS Energy Lett.* **2019**, *4*, 2913.
[38] a) J. Liang, X. Hu, C. Wang, C. Liang, C. Chen, M. Xiao, J. Li, C. Tao, G. Xing, R. Yu, *Joule* **2022**, *6*, 816; b) J. D. McGettrick, K. Hooper, A. Pockett, J. Baker, J. Troughton, M. Carnie, T. Watson, *Mater. Lett.* **2019**, *251*, 98.
[39] J. H. Scofield, *J. Electron Spectrosc. Relat. Phenom.* **1976**, *8*, 129.
[40] A. M. Boehm, J. Wieser, K. Butrouna, K. R. Graham, *Org. Electron.* **2017**, *41*, 9.
[41] I. Chung, J. H. Song, J. Im, J. Androulakis, C. D. Malliakas, H. Li, A. J. Freeman, J. T. Kenney, M. G. Kanatzidis, *J. Am. Chem. Soc.* **2012**, *134*, 8579.
[42] Q. Wang, Y. Shao, H. Xie, L. Lyu, X. Liu, Y. Gao, J. Huang, *Appl. Phys. Lett.* **2014**, *105*, 163508.
[43] K. T. Cho, G. Grancini, Y. Lee, E. Oveisi, J. Ryu, O. Almora, M. Tschumi, P. A. Schouwink, G. Seo, S. Heo, *Energy Environ. Sci.* **2018**, *11*, 952.
[44] A. Delmastro, D. Mazza, S. Ronchetti, M. Vallino, R. Spinicci, P. Brovetto, M. Salis, *Mater. Sci. Eng. B* **2001**, *79*, 140.

[45] a) T. L. Leung, Z. Ren, A. A. Syed, L. Grisanti, A. B. Djurišić, J. Popović, *ACS Energy Lett.* **2022**, *7*, 3500; b) S. J. Yang, K. Wang, Y. Luo, J. Y. Park, H. Yang, A. H. Coffey, K. Ma, J. Sun, S. Wieghold, C. Zhu, *ACS Energy Lett.* **2023**, *8*, 3693.

[46] T. Hu, M. D. Smith, E. R. Dohner, M.-J. Sher, X. Wu, M. T. Trinh, A. Fisher, J. Corbett, X.-Y. Zhu, H. I. Karunadasa, *J. Phys. Chem. Lett.* **2016**, *7*, 2258.

[47] a) E. S. Parrott, R. L. Milot, T. Stergiopoulos, H. J. Snaith, M. B. Johnston, L. M. Herz, *J. Phys. Chem. Lett.* **2016**, *7*, 1321; b) D. W. de Quilettes, S. M. Vorpahl, S. D. Stranks, H. Nagaoka, G. E. Eperon, M. E. Ziffer, H. J. Snaith, D. S. Ginger, *Science* **2015**, *348*, 683.

[48] Y. Jiang, M. Cui, S. Li, C. Sun, Y. Huang, J. Wei, L. Zhang, M. Lv, C. Qin, Y. Liu, *Nat. Commun.* **2021**, *12*, 336.

[49] G. Delport, G. Chehade, F. Lédée, H. Diab, C. Milesi-Brault, G. Trippé-Allard, J. Even, J.-S. Lauret, E. Deleporte, D. Garrot, *J. Phys. Chem. Lett.* **2019**, *10*, 5153.

[50] a) L. Dou, A. B. Wong, Y. Yu, M. Lai, N. Kornienko, S. W. Eaton, A. Fu, C. G. Bischak, J. Ma, T. Ding, *Science* **2015**, *349*, 1518; b) H. Guthrey, J. Moseley, *Adv. Energy Mater.* **2020**, *10*, 1903840.

[51] F. Yuan, X. Zheng, A. Johnston, Y.-K. Wang, C. Zhou, Y. Dong, B. Chen, H. Chen, J. Z. Fan, G. Sharma, *Sci. Adv.* **2020**, *6*, abb0253.

[52] K. Wang, C. Wu, Y. Jiang, D. Yang, K. Wang, S. Priya, *Sci. Adv.* **2019**, *5*, aau3241.

[53] a) D. J. Kubicki, D. Prochowicz, E. Salager, A. Rakhmatullin, C. P. Grey, L. Emsley, S. D. Stranks, *J. Am. Chem. Soc.* **2020**, *142*, 7813; b) T. Leijtens, R. Prasanna, A. Gold-Parker, M. F. Toney, M. D. McGehee, *ACS Energy Lett.* **2017**, *2*, 2159.